RSC Advances

PAPER

View Article Online
View Journal | View Issue

Cite this: *RSC Adv.*, 2026, **16**, 23963

Electronic transport in radial π-conjugated macrocyclic molecules: a density functional theory study

Sneigitha Govindarajan, [a] Kunchanapalli Ramya,[a] Mahesh Kumar Ravva †*[b] and Sabyasachi Mukhopadhyay *[a]

Radially conjugated macrocyclic molecules offer a unique approach to tuning frontier orbital energies by manipulating ring geometry and donor–acceptor (D–A) interactions. Here, we present a systematic DFT study of the electronic structure and metal-molecule energy-level alignment for a series of macrocyclic molecules and their linear counterparts, which include thiophene, diketopyrrolopyrrole (DPP), benzodithiophene (BDT), dithienobenzodithiophene (DTBDT), and benzothiazole (BT) units. Our calculations indicate that macrocyclization induces a system-specific change in the HOMO–LUMO energy gap, with the direction and magnitude depending on the balance between ring strain and D–A coupling strength for each molecule. Among the studied systems, $[DTBDT\text{-}DPP]_3$ has the smallest HOMO–LUMO gap, decreasing from 1.13 eV in the isolated macrocycle to 1.44 eV in the Au18 junction model due to electrode-induced orbital hybridization. Its HOMO at −5.31 eV aligns most closely with the Au18 Fermi level, resulting in a hole injection barrier. (Φ_h) of approximately 0.01–0.21 eV, making it the most promising candidate for hole injection in this series. These results establish quantitative structure–property relationships across five D–A macrocyclic architectures and offer a computational foundation for the rational design of macrocycle-based organic semiconductors.

Received 19th February 2026
Accepted 27th April 2026

DOI: 10.1039/d6ra01456a

rsc.li/rsc-advances

Introduction

In the current generation of organic electronics, π-conjugated macrocycles have attracted considerable interest in organic electronics owing to their unique radially delocalized π-electron systems, which establish closed-loop conjugation pathways not accessible in linear architectures.[1] Unlike linear oligomers, where free rotation around inter-ring σ-bonds generates a distribution of dihedral angles that disrupts conjugation, macrocycles enforce a fixed ring topology that constrains inter-ring dihedral angles and supports a continuous circumferential π-conjugation pathway. Significant progress has been made in developing D–A macrocyclic systems based on cyclo-paraphenylene (CPP), porphyrin nanoring, and conjugated cyclooligothiophenes, in which radial π-delocalization gives rise to distinctive photophysical behaviour.[2,3] However, systematic computational studies comparing linear and macrocyclic D–A topologies, particularly for structures interfaced with metal electrodes, remain scarce, and the relationship between macrocyclic architecture and metal-molecule energy-level alignment is not well established.

The thiophene-based units are widely recognized for enhancing conjugation and stability in linear polymers. Yet, their integration into macrocycles to optimize D–A interactions and charge delocalization has not been systematically studied.[4] Thiophene enhances conjugation,[5] chemical stability,[5,6] and hole mobility in linear conjugated systems.[7] Its integration into macrocycles could amplify these benefits while mitigating steric strain.[8,9] It is important to note that radial π-conjugated macrocycles, such as the hoop-shaped system studied here, are fundamentally distinct from planar π-macrocycles. In the radially conjugated macrocycles, the constituent aromatic rings are arranged tangentially around the ring circumference, with their p-orbitals directed radially pointing towards the interior and exterior of the macrocycle. This contrasts with planar macrocycles such as porphyrins, in which the molecule is flat, and the π-orbitals extend above and below the molecular skeleton in the conventional sense. Among radial π-conjugated macrocyclic systems, cycloparaphenylene (CPP) has been widely studied, in which aromatic units are linked in a hoop-shaped arrangement.[10] Inspired by these hoop-shaped moieties, in our study, we aim to develop macrocyclic π-conjugated molecules using diketopyrrolopyrrole (DPP) as a core unit. DPP is a well-established electron-deficient building block known for

[a]*Department of Physics, SRM University-AP, Amaravati, Andhra Pradesh-522240, India. E-mail: sabyasachi.m@srmap.edu.in*

[b]*Department of Chemistry, SRM University-AP, Amaravati, Andhra Pradesh-522240, India. E-mail: mahesh.r@srmap.edu.in*

† Author also affiliated with Centre for Computational and Integrative Sciences (CCIS) and Centre for Interdisciplinary Research, SRM University-AP, Amaravati Andhra Pradesh-522240, India.

its ability to fine-tune optoelectronic properties when paired with electron-donating units.[1,11–13] It has been successfully applied in organic transistors as both p-type and n-type semiconductor materials.[14–16]

While macrocyclic architectures are known to confer benefits such as planarity and intramolecular ordering, very few studies explore the effects of DPP-based macrocycles on electron injection and transport in device-like junctions.[17] Thus, the electronic properties of DPP can be further modulated by pairing with benzodithiophene (BDT),[18] dithienobenzodithiophene (DTBDT),[19] and benzothiazole (BT)[20] each bringing a distinct donor or acceptor strength. However, the behaviour of these units when embedded in macrocyclic *vs.* linear topologies remains a question of both theoretical and practical importance. In linear conjugated oligomers, free rotation around inter-ring bonds produces a distribution of inter-ring dihedral angles, which disrupts π-orbital overlap and leads to non-uniform conjugation along the backbone. Macrocyclization restricts this rotational freedom by imposing geometric closure, which narrows the accessible range of inter-ring dihedral angles and thereby supports a more continuous π-conjugation pathway around the ring.[9] However, the same geometric constraint introduces ring strain, which can force the inter-ring bonds out of planarity, partially reducing the electronic benefit of cyclization. The strain conjugation trade-off was examined systematically across the five molecular systems in this study.[9,10] In recent years, thiophene-based conjugated materials have attracted sustained interest in organic electronics owing to their favourable electronic properties, chemical stability, and thermal robustness.[4,10,21] and have been utilized in highly efficient, polymer-based, and small-molecule organic photovoltaic devices.[22,23]

Although fullerene-based materials are used in photovoltaics for their electronic acceptor behaviour, the compounds are unstable when formed in thin films.[24–26] Thus, non-fullerene acceptor (NFA) moieties, such as DPPs, are used to address key challenges in the rational design of π-conjugated macrocycles for optoelectronic applications. The synergy between the electronic levels of DPP and donor units such as thiophene, TT, BDT, and DTBDT in macrocyclic geometries is poorly understood and rarely benchmarked against linear analogs.[9,14,27] Although NFAs have matured in linear designs, macrocyclic NFAs with tuneable LUMO levels, photostability, and potential for device integration remain underutilized.[24,25,28] Beyond the effects of NFAs, the influence of macrocyclic curvature and radial conjugation on the energy-level alignment, orbital distribution, and interfacial energetics of macrocycles incorporated into metal-molecule junctions has remained underexplored for decades.[25,29] Thus, to contribute to this evolving field, we conducted a theoretical investigation of the charge-transport behaviour of both linear and macrocyclic structures incorporating key D–A building blocks. The linear system includes a thiophene-based polymer chain with 10 repeating units, denoted as $[PT]_{10}$. The macrocyclic systems contain three repeating units of various aromatic moieties, including bithiophene (TT), benzodithiophene (BDT), dithienobenzodithiophene (DTBDT), diketopyrrolopyrrole (DPP), and benzothiazole (BT). They are denoted as $[TT\text{-}DPP]_3$, $[BDTDPP]_3$, $[DTBDT\text{-}DPP]_3$, and $[DTBDT\text{-}BT]_3$, respectively. Using first-principles DFT calculations,[30] we study how structural variations influence HOMO–LUMO energy levels and their effects on electron transport characteristics in macrocycle-based molecular junctions. The hoop-shaped macrocycles studied here establish a closed-loop circumferential conjugation pathway that has no equivalent in linear architectures. Embedding the BT and DPP acceptor units within this macrocyclic backbone introduces the D–A character that shifts the HOMO and LUMO energies and redistributes the frontier orbital density across the donor and acceptor fragments, as quantified by the DFT calculations in this work and illustrated by the HOMO and LUMO isosurface plots, which have been provided in Fig. S1 of the SI. Our findings establish quantitative structure–property relationships across five D–A macrocyclic architectures and provide a computational basis for guiding the rational design of macrocycle-based organic semiconductor candidates.

Computational details

Geometry parameters

Thiophene units, rich conjugated molecules, are promising materials in the field of molecular electronics because of their ease of synthesis, prominence, and chemical stability.[31,32] In this work, we theoretically investigate how the number of thiophene units and the incorporation of other aromatic units, such as DPP and BT, into hoop-shaped macrocycles influence the HOMO–LUMO energy levels, thereby modulating electron-transport properties. To explore these properties, we performed geometry optimization simulations using Density Functional Theory (DFT) as implemented in the Gaussian 16 package (29). The hybrid PBE0 functional was chosen for geometry optimization due to its validated accuracy in predicting electronic structures of conjugated organic systems, particularly for HOMO–LUMO gaps and π-orbital delocalization.[33,34] For charge transport calculations, the PBE0 hybrid exchange–correlation functional was employed, as it reliably models metal-molecule interfaces and electron transport in junctions, consistent with prior studies[35] on Au-thiophene systems. The 6-31G** basis set with polarization functions (d-orbitals on C, S, and N) was used for macrocyclic molecules to accurately describe valence-electron behaviour and π-conjugation effects, a standard choice for organic systems. To achieve scalar relativistic effects, effective core potentials (ECPs) are combined with the LANL2DZ basis set for gold clusters. Each macrocycle molecule was anchored to an Au18 truncated decahedral nanocluster *via* the Mark's decahedral geometry on both sides, *via* Au–S bonds at the terminal sulphur atoms of the thiophene units.[36–38] The cluster consists of 18 gold atoms in a truncated decahedral arrangement with an Au–Au bond length of 2.88 Å and approximate C_{2v} local symmetry. This geometry was taken from the model established by Quek *et al.*[38] and Mori & Hegmann,[37] which has been validated as a finite-cluster electrode model that replicates the local atomic coordination environment and work function of the Au (111)

surface. The cluster was re-optimized at the PBE0/LANL2DZ level of theory in Gaussian 16, the optimized cartesian coordinates are provided in the SI[37,38](SI page, no 3–4) thus, for the molecular junction (macrocycle + Au electrodes), the GENECP mixed basis set combined LANL2DZ for Au and 6-31G** for light atoms, ensuring accuracy at the molecule-electrode interface without prohibitive computational costs. In transport calculations, a Single Zeta Polarization (SZP) basis set for Au valence electrons simplified the modeling of metallic states. In contrast, a Double Zeta Polarization (DZP) basis set for other atoms resolved molecular orbitals effectively. The Landauer-Büttiker formalism[39] provides the theoretical framework for conductance calculations in such metal–molecule junctions, and full NEGF-DFT transport calculations based on the junction geometries established here are identified as a direction for future work. [SI page, no 2–3].

Results and discussion

π-Conjugated linear structure and radial macrocyclic structure

The linear and macrocyclic compounds of $[PT]_{10}$, $[TT\text{-}DPP]_3$, $[BDT\text{-}DPP]_3$, $[DTBDT\text{-}DPP]_3$, and $[DTBDT\text{-}BT]_3$ were optimized with 2 and 3 repeating units, and dihedral angles were obtained at the M062X/6-31G** and PBE0/6-31G** levels of theory. Table 1 reports the macrocyclic ring radius and the inter-thiophene distance in the linear form for each compound, both measured between the two adjacent thiophene units at the PBE0/6-31G** level of theory. These values serve as geometric structural descriptors, characterizing the molecular dimensions imposed by each combination of repeat units and the spatial extent of the conjugation pathway in each topology.[40,41] For $[PT]_{10}$, the macrocyclic ring radius is 6.2 Å and the linear inter-thiophene distance is 17.3 Å (Fig. 1). This difference reflects the geometric consequences of the ring closure; the macrocyclization redirects the π-conjugation pathway from the extended linear backbone to a closed-loop, circumferential geometry. How this topological change affects the HOMO–LUMO gap and frontier orbital distribution is established by the DFT calculations in Table 2, which are discussed in the following section.

The macrocyclic radius of $[TT\text{-}DPP]_3$ (6.02 Å) closely mirrors that of $[PT]_{10}$ (6.2 Å), a result of the comparable spatial dimensions of the bithiophene and thiophene repeat units rather than any electronic effect. While DPP is electron-deficient and imparts D–A character to the backbone, it functions as a compact bridging unit between two TT donors. It contributes minimally to the overall ring circumference. For $[BDT\text{-}DPP]_3$, the macrocyclic radius of 6.09 Å and linear inter-thiophene distance of 17.3 Å indicate that substituting TT with BDT leaves the ring circumference essentially unchanged, as both donors occupy a similar molecular footprint within the ring. The electronic consequences of this substitution, however, are significant: the HOMO–LUMO gap narrows from 2.10 eV in the linear form to 1.83 eV upon macrocyclization of $[BDT\text{-}DPP]_3$. This reduction is attributed to the structural rigidity of the fused BDT aromatic framework, which constrains inter-ring torsional

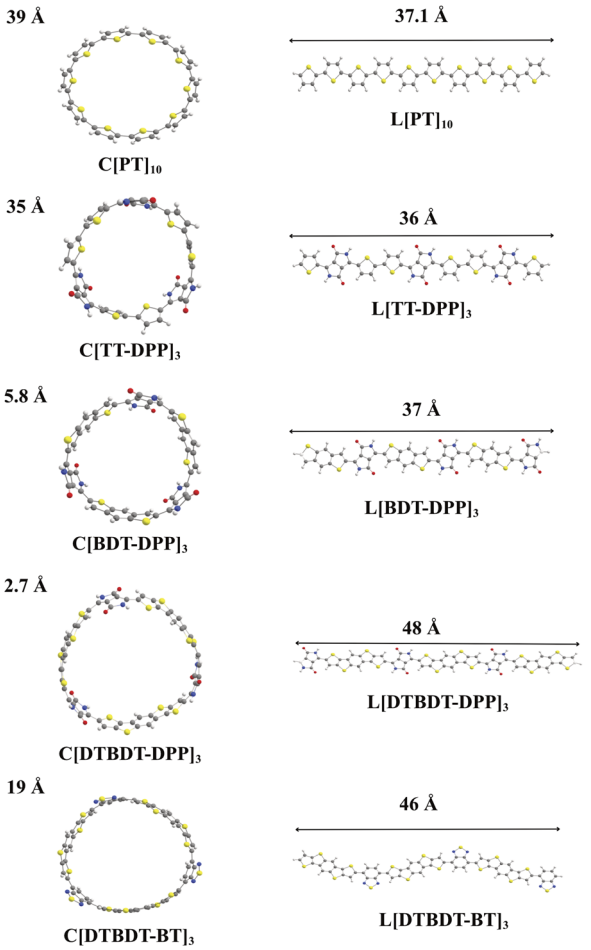

Fig. 1 PBE0/6-31G**-optimized structures of the macrocyclic (left) and linear (right) forms of $[PT]_{10}$, $[TT\text{-}DPP]_3$, $[BDT\text{-}DPP]_3$, $[DTBDT\text{-}DPP]_3$, and $[DTBDT\text{-}BT]_3$, illustrating the geometric differences in ring circumference and molecular dimensions across the series. Atom colour codes are: yellow-sulphur, grey-carbon, white-hydrogen, blue-nitrogen, red-oxygen.

Table 1 Representation of radii of the macrocyclic and linear structure of the $[PT]_{10}$, $[TT\text{-}DPP]_3$, $[BDT\text{-}DPP]_3$, $[DTBDT\text{-}DPP]_3$, and $[DTBDT\text{-}BT]_3$ molecules

Compound	Macrocyclic structure (Å)	Linear structure (Å)
$[PT]_{10}$	6.2	17.3
$[TT\text{-}DPP]_3$	6.02	16.8
$[BDT\text{-}DPP]_3$	6.09	17.3
$[DTBDT\text{-}DPP]_3$	7.79	23.0
$[DTBDT\text{-}BT]_3$	7.57	22.0

angles toward coplanarity and strengthens intramolecular π-orbital overlap, an effect that is absent in the more conformationally flexible TT-based system and is discussed in detail in the HOMO–LUMO analysis below. The $[DTBDT\text{-}DPP]_3$ has the macrocyclic radius of 7.79 Å, larger than those of the $[TT\text{-}DPP]_3$ and $[BDT\text{-}DPP]_3$ contains 6.02 Å and 6.09 Å, which are 6.02 Å and 6.09 Å, respectively, owing to the spatial extent of the

Table 2 Representation of HOMO, LUMO, and bandgap values of linear and macrocyclic structures of molecules $[PT]_{10}$, $[TT\text{-}DPP]_3$, $[BDT\text{-}DPP]_3$, $[DTBDT\text{-}DPP]_3$, and $[DTBDT\text{-}BT]_3$ by using PBE0/6-31G**

	Linear structure			Macrocyclic structure		
Compound	HOMO (eV)	LUMO (eV)	E_g (eV)	HOMO (eV)	LUMO (eV)	E_g (eV)
$[PT]_{10}$	−4.98	−2.22	2.76	−5.30	−1.69	3.61
$[TT\text{-}DPP]_3$	−5.14	−3.25	1.89	−5.26	−3.16	2.10
$[BDT\text{-}DPP]_3$	−5.31	−3.26	2.03	−5.31	−3.47	1.83
$[DTBDT\text{-}DPP]_3$	−5.28	−3.18	2.10	−5.27	−3.29	1.97
$[DTBDT\text{-}BT]_3$	−5.28	−2.95	2.33	−5.17	−3.05	2.11

DTBDT unit. The DTBDT consists of four thiophene rings fused around a central benzene core, which gives a larger molecular footprint than the $[TT\text{-}DPP]_3$ and $[BDT\text{-}DPP]_3$. The increased ring radius extends the closed-loop circumferential π-conjugation pathway relative to the smaller $[TT\text{-}DPP]_3$- and $[BDT\text{-}DPP]_3$-based molecules. Similarly, the macrocyclic radius of $[DTBDT\text{-}BT]_3$ is calculated to be 7.57 Å, whereas the linear structure has a dihedral angle of 22 Å. The larger macrocyclic radius of $[DTBDT\text{-}BT]_3$ (7.57 Å) relative to TT- and BDT-based systems reflects the greater physical size of the DTBDT donor unit. The smaller ring radii of TT- and BDT-containing macrocycles (6.02–6.09 Å) compared to their linear end-to-end distances (16.8–17.3 Å) confirm that macrocyclization compresses the conjugation pathway from a linear chain into a compact closed-loop geometry. The systematic difference in molecular dimensions between the linear and macrocyclic forms of each compound quantifies the geometric consequence of ring closure across the five systems studied. The macrocyclic radii of 6.02–7.79 Å confirm that ring closure produces a compact circumferential molecular geometry in all five systems; the electronic consequences of this geometric change are established separately by the DFT calculated HOMO–LUMO gap values in Table 2. The constrained ring geometry enforces fixed inter-ring dihedral angles between adjacent aromatic units, strengthening intramolecular electronic coupling between donor and acceptor fragments within the closed-loop backbone. In linear structures, conjugation extends along the molecular backbone due to the greater conformational freedom available to inter-ring single bonds, as reflected in the larger inter-thiophene distances of 16.8–23 Å. The molecular ring radius increases systematically with the spatial extent of the donor unit. PT and TT/BDT-based macrocycles have radii of 6.02–6.2 Å, while the bulkier DTBDT-containing macrocycles have radii of 7.57–7.79 Å, consistent with the four-ring fused structure of the DTBDT unit.

This steric bulk introduces conformational flexibility, leading to a partial loss of planarity in macrocyclic structures. The cyclic geometry enforces fixed inter-ring dihedral angles within each repeat unit, maintaining consistent intramolecular electronic coupling between the adjacent aromatic units around the ring. The interplay among ring strain, inter-ring dihedral-angle constraints imposed by macrocyclization, and the spatial extent of the constituent aromatic units collectively determines the geometric framework within which the electronic structure, and hence the optoelectronic properties, of these macrocyclic systems are established.

To study the tunability of the electronic properties of π-conjugated macrocyclic molecules, we have calculated the highest occupied molecular orbital (HOMO) and lowest unoccupied molecular orbital (LUMO) levels using DFT.[42] The energy band gap (E_g), determined by the difference between the HOMO and LUMO, influences charge transport and optical absorption in these macrocyclic systems.[1] Several factors govern this gap: the extent of π-conjugation, molecular planarity, structural strain, and electronic interactions between donor and acceptor units.[43] From Table 2 and Fig. 2, we observed that the bandgap values of macrocyclic structures are lower than those of their linear counterparts. The macrocyclic molecules have a molecule-dependent effect on the energy bandgap; for $[BDT\text{-}DPP]_3$, $[DTBDT\text{-}DPP]_3$, and $[DTBDT\text{-}BT]_3$, the bandgap is reduced relative to the linear counterpart. In contrast, for $[PT]_{10}$ and $[TT\text{-}DPP]_3$, the macrocyclic form exhibits the larger energy bandgap. This divergence reflects the complex interplay between the degrees of ring strain and planarity, and the strength of the donor–acceptor coupling in the molecular system.[44]

Ring closure imposes geometric strain on the macrocyclic backbone by forcing aromatic units into a curved, non-planar arrangement. This ring strain distorts inter-ring dihedral angles away from the coplanar geometry that maximizes π-orbital overlap, reducing the effective conjugation length and increasing the HOMO–LUMO gap. In systems where the ring circumference is large enough to accommodate the constituent aromatic units without significant angular distortion, as in the BDT and DTBDT containing macrocycles, the geometric constraint of ring closure instead enforces near coplanar inter-

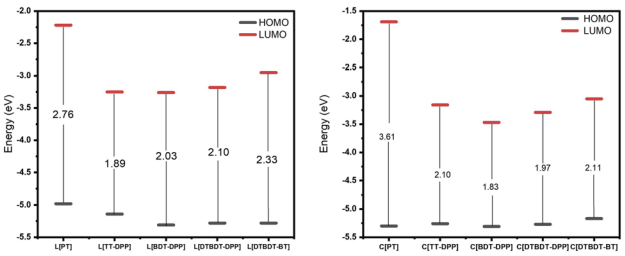

Fig. 2 Representation of HOMO, LUMO, and energy bandgap of linear and macrocyclic structures of the molecules $[PT]_{10}$, $[TT\text{-}DPP]_3$, $[BDT\text{-}DPP]_3$, $[DTBDT\text{-}DPP]_3$, and $[DTBDT\text{-}BT]_3$.

ring dihedral angles, enhancing conjugation relative to the freely rotating linear analog and narrowing the bandgap.[45] From Table 2, we observed that the thiophene $[PT]_{10}$ system exhibits the highest bandgap value among all molecules in the range of 3.61 eV in its macrocyclic form ($C[PT]_{10}$) compared to 2.76 in its linear form ($L[PT]_{10}$). This increased bandgap value in the macrocyclic form is due to polythiophene $[PT]_{10}$, which induces ring strain by distorting the ring from planarity. This distortion in planarity is caused by the rigidity of the twelve-membered rings in the closed loop, which in turn disrupts the π-orbital overlap that is necessary for efficient conjugation. $[PT]_{10}$ also lacks strong electron-donating or electron-accepting groups that are responsible for the stabilization of the HOMO and LUMO levels, resulting in the high-lying LUMO (−1.69 eV) that directly contributes to the large bandgap value. Whereas the DPP-based systems, including $[TT\text{-}DPP]_3$, $[BDT\text{-}DPP]_3$, and $[DTBDT\text{-}DPP]_3$, exhibit reduced bandgap values that enhance electronic properties compared to $[PT]_{10}$. This reduction in bandgap values is primarily due to their donor–acceptor molecular architecture. Among all the DPP-based molecules, the $[TT\text{-}DPP]_3$ cyclic structure shows a higher bandgap value of 2.2 eV, compared to its linear counterpart of 1.89 eV. This increase in bandgap is due to two key factors, including (a) the process of macrocyclization imposes rotational restriction at the thiophene-DPP junctions, potentially enforcing non-optimal dihedral angles that hinder effective π-conjugation, leading to an increase in bandgap value. And (b) by effecting electron delocalization across the molecule, the spatial limitation reduces the overlap between adjacent orbitals that results in the largest bandgap value. Thus, the thiophene entities in TT-DPP act as medium electron donors. The strength of the medium donor produces a less pronounced donor–acceptor interaction with DPP units compared to molecules that incorporate more extended π-conjugated systems or stronger electron-donating groups. Thus, the combined structural and electronic effects result in an increased bandgap value in the C[TT-DPP] macrocycle. Among all the molecules, $[BDT\text{-}DPP]_3$ has a lower bandgap of 1.83 eV, compared to its linear architecture at 2.03 eV. Thus, by incorporating fused aromatic rings that compel molecular planarity, the BDT unit plays a crucial role in macrocyclic systems. The π-orbital overlap and electron delocalization along the conjugated entities are enhanced due to the reduction of torsional angles between the adjacent units caused by the structural rigidity. Compared to the pristine thiophene-based system, the fused BDT system exhibits extended conjugation, offering a broader π-electron delocalization pathway that reduces the effective optical gap. Since the inherent ring enhances π-conjugation, the C[BT-DPP] unit achieves an optimal balance, unlike other macrocycles, where ring strain disrupts conjugation. This disruption is due to the difference between the lowered LUMO value in the macrocyclic form (−3.47 eV) and that of linear architectures (−3.26 eV), which leads to a stabilized electronic structure and improved electron affinity. Thus, our study reveals prominent electronic properties of the C[BDT-DPP] macrocycle, including a reduced bandgap. Similarly, the C[DTBDT-DPP] system exhibits a slightly lower band gap of 1.97 eV compared to linear architectures (2.10 eV). Since the bandgap difference is less, the C[DTBDT-DPP] system exhibits equivalent electronic properties of cyclic and linear architectures. This is nearly equivalent to the electronic properties of the linear and cyclic forms, suggesting a unique interaction between conjugation and structural strain. The DTBDT unit incorporates additional thiophene rings fused to the benzodithiophene core, resulting in an extensive π-conjugated system. This structural feature enhances electronic delocalization throughout the molecule, which is typically associated with macrocyclic systems. As a result, the electronic characteristics of the cyclic forms remain closely aligned with the linear structure, reflecting a well-balanced interaction between conjugation and strain in the C[DTBDT-DPP] system. On the other hand, the DTBDT molecule is introduced with benzothiazole (BT) as an acceptor unit in place of DPP, thereby indicating changes in the electronic properties. The higher bandgap is observed in the cyclic form of coupling, which contributes to the relatively higher bandgap of the [DTBDT-BT] system, measured at 2.11 eV. We have observed the discrepancy between the macrocyclic and linear forms of the molecule. The energy gap of the linear form is recorded at 2.33 eV, which is significantly higher than that of the macrocyclic form, with a difference of 0.22 eV. This difference suggests that the cyclic structure enhances the radial conjugation. This improvement is likely due to the planarity induced by the cyclic structure, which effectively counteracts the inherent flexibility of the BT linkage and promotes a more delocalized electronic system. One difference between the BT and DPP is their acceptor strength. Benzothiazole is generally a weaker electron acceptor than DPP, resulting in weaker donor–acceptor interactions within the molecule. This reduced electronic coupling contributes to the increased bandgap. Thus, from the DFT calculations, the frontier molecular orbitals are affected differently by the macrocyclic architecture. The macrocyclic configuration creates additional pathways for π-electron delocalization but also introduces geometric constraints. The HOMO is well distributed across the entire π-system, especially in the electron-rich donor units (thiophene derivatives). In contrast, the LUMO tends to concentrate on the electron-deficient acceptor units (DPP and BT), thereby facilitating intramolecular charge transport upon excitation. The closed-loop configuration in macrocyclic structures provides a pathway for π-electron delocalization, thereby enhancing electronic coupling between repeating units. The comparative analysis of cyclic and linear π-conjugated systems reveals various relationships between structure and properties. Optimal electronic properties are derived from balancing conjugation against the induced structural strain in cyclic compounds. By achieving lower band gaps through enhanced electronic coupling, the C[DTBDT-DPP]-conjugated macrocycle exhibits well-structured donor–acceptor systems compared with linear architectures. The linear and macrocyclic structures of $[PT]_{10}$, $[TT\text{-}DPP]_3$, $[BDT\text{-}DPP]_3$, $[DTBDT\text{-}DPP]_3$, and $[DTBDT\text{-}BT]_3$ exhibit different trends in the electronic properties, especially in the values of bandgap. The bandgap values increase sharply from 2.76 to 3.7 eV, corresponding to a 30.8% rise in the $[PT]_{10}$ macrocyclic structure. In the case of $[TT\text{-}DPP]_3$, the bandgap increased moderately by

11%, *i.e.*, from 1.89 to 2.10 eV, upon conversion from linear architectures to its macrocyclic form. Conversely, a reduction in bandgap values is observed for the $[BDT\text{-}DPP]_3$, $[DTBDT\text{-}DPP]_3$, and $[DTBDT\text{-}BT]_3$ macrocyclic conjugated structures. The observed discrepancies in bandgap values across all conjugated macrocycles, both linear and cyclic, are consistent with band diagrams showing shifts in the HOMO and LUMO energy levels. The interplay between molecular planarity and macrocyclic ring strain affects changes in bandgap values. Macrocycles with higher ring strain induce deviations from planarity and alter electronic delocalization, thereby reducing the bandgap. These results highlight the effect of macrocyclization on the bandgap, which can widen or narrow depending on the specific molecular framework and its ability to accommodate strain without significant loss of conjugation.

From the DFT analysis of the five macrocyclic molecules shown in Mulliken charge distribution Fig. 3 and the corresponding electronic data Table 2, we have observed a clear correlation between the spatial charge distribution patterns and the HOMO–LUMO electronic properties. The results reveal fundamental structure–property relationships that govern the optoelectronic behaviour of these donor–acceptor-conjugated systems.

The colour configuration in the charge distribution visualizations follows a systematic pattern: red and brown regions represent higher negative charge density, indicating electron-rich zones that typically correspond to donor segments of the molecules. In comparison, the green regions represent areas of lower electron density or more positive charge character, indicating electron-deficient zones that typically correspond to acceptor segments. From the homopolymer polythiophene to the complex donor–acceptor architectures, the variation in the pattern of electron-poor and electron-rich regions becomes increasingly pronounced when correlated with changes in bandgap values.

As shown in Fig. 3, polythiophene [PT] exhibits a uniform charge distribution predominantly throughout the thiophene rings, as indicated by the red and blue colours. This charge distribution indicates electronic distribution within the sulphur-containing aromatic framework, further supported by the largest energy gap of 3.61 eV, with a HOMO at −5.30 eV and a LUMO at −1.69 eV. This wide bandgap results from the absence of a strong electron-accepting unit and could be considered as one of the homopolymer characteristics. The [TT-DPP] system (structure b) shows an enhanced degree of electronic transition, with distinct red and brown regions corresponding to the electron-rich bithiophene donor segments and green regions indicating the electron-deficient diketopyrrolopyrrole acceptor units. This charge separation pattern correlates with a significantly reduced energy gap of 2.10 eV (HOMO −5.26 eV, LUMO −3.16 eV), demonstrating that the donor–acceptor architecture facilitates intramolecular charge transfer, thereby narrowing the band gap. The [BDT-DPP] system (structure c) exhibits the most dramatic charge separation, with strongly contrasting red, brown, and green regions. This enhanced degree of electronic transition corresponds to the smallest energy gap in the series, at 1.83 eV, with the most negative LUMO energy at −3.47 eV and a HOMO energy at −5.31 eV, indicating that the benzodithiophene donor, combined with the diketopyrrolopyrrole acceptor, creates the most effective charge-transfer system among the molecules studied. The [DTBDT-DPP] system (structure d) shows a similar but slightly less pronounced charge transition pattern compared to BDT-DPP, which correlates with its slightly larger energy gap of 1.97 eV (HOMO −5.27 eV, LUMO −3.29 eV). In contrast, the [DTBDT-BT] system (structure e) displays an alternating pattern with less dramatic contrast between electron-rich and electron-poor regions than the DPP-based systems, corresponding to its energy gap of 2.11 eV (HOMO −5.17 eV, LUMO −3.05 eV). The mechanistic understanding of these correlations reveals that the red and brown regions in the charge distribution maps correspond to areas where the HOMO is primarily localized, as these electron-rich donor segments readily provide electrons for oxidation or hole transport. In contrast, the green regions correspond to areas of LUMO localization, where the electron-deficient acceptor units can readily accept electrons during reduction processes or electronic transitions. The extent of charge separation correlates with reduced bandgap values, as visualized by colour contrast in Mulliken analysis. A sharper contrast between the electron-rich (red) and electron-deficient (green) regions in Mulliken charge maps indicates a stronger intramolecular charge transfer (ICT) character, with electron density shifting from the donor fragment to the acceptor fragment within the same molecule. This redistribution lowers the LUMO energy by concentrating it on the electron-deficient acceptor unit and raises the HOMO energy by concentrating it on the electron-rich donor unit. The net effect is a narrower HOMO–LUMO gap in molecules where D–A coupling is strong. While maintaining the orbital overlap necessary for electronic coupling, the spatial separation of HOMO and LUMO densities characteristic of D–A intramolecular charge transfer (ICT) systems is particularly relevant for organic photovoltaic (OPV) applications, where it facilitates broad spectral absorption and promotes efficient exciton dissociation at heterojunctions. This is a well-established design principle in non-fullerene acceptors (NFAs). The calculated HOMO–LUMO density distribution identifies the spatial

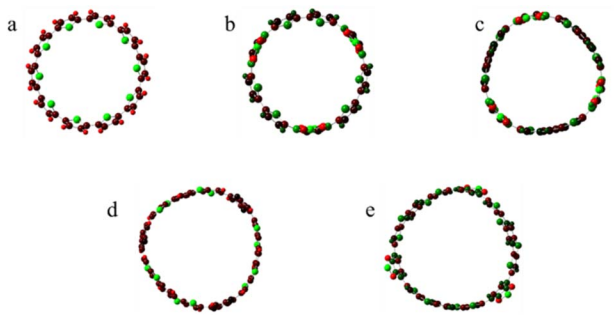

Fig. 3 Mulliken charge distribution of molecules (a) $[PT]_{10}$, (b) $[TT\text{-}DPP]_3$, (c) $[BDT\text{-}DPP]_3$, (d) $[DTBDT\text{-}DPP]_3$, and (e) $[DTBDT\text{-}BT]_3$. The charge distribution visualizations follow a systematic colour scale: red/brown = electron-rich regions (donor segments) and green = electron-deficient regions (acceptor segments).

localization of electron-rich (donor) and electron-deficient (acceptor) regions within the molecule and quantifies ICT character. When the HOMO is localized on the donor fragment and the LUMO on the acceptor fragment, the molecule exhibits ground-state charge separation and a low-energy ICT absorption band with measurable oscillator strength. Both properties are relevant to OPV performance, which requires a low optical gap and efficient photoinduced charge separation. In molecular junction calculation, HOMO and LUMO density toward the anchoring sulphur atoms set the electronic coupling (Γ) at the metal-molecule interface, governing the charge injection barrier ($\Phi = |E_{FMO} - E_F|$) and the transmission probability at the Fermi level.

To understand the effect of molecule-electrode coupling on frontier orbitals, we designed a macrocycle-based molecular junction by adding macrocyclic molecules to gold electrodes. Thus, Fig. 4 depicts macrocyclic molecular junctions in which various molecules incorporating thiophene units, such as TT, BDT, DTBDT, and electron-accepting units like DPP and BT, that differ in their central conjugated systems, are attached to gold nanocrystals. Through the orbital hybridization, Fermi level alignment, and the Au18 Marks decahedron clusters induce significant changes in the intramolecular charge transfer character and frontier orbital energies of the macrocycle. The macrocycle is anchored to the Au18 cluster through Au–S bonds formed at the terminal sulphur atoms of the thiophene units. This Au–S contact geometry is the model used throughout our calculations. Experimentally, however, gold can also bind directly to the aromatic ring carbons rather than to sulphur, forming Au-π contacts.[46] Such contacts have been reported in macrocyclic junction measurements and can alter the metal-molecule coupling strength; in some cases, they promote ring-opening of the macrocycle. Modelling these alternative binding geometries requires a separate computational calculation, and it is left for future work. Upon geometry optimization of each molecular junction at the PBE0/GENECP level of theory, the Au18 electrode cluster undergoes local structural relaxation at the molecule-electrode interface.binding site specifically, Au atoms directly bonded to the sulphur anchor exhibit elongation of Au–Au distances relative to pristine cluster driven by the formation of the Au–S covalent bond at the Sulphur anchor atom of the macrocycle. Specifically, the two apical Au atoms in direct contact with the sulphur anchor sites elongate their Au–Au bond distances relative to the pristine Au18 cluster (Au–Au = 2.88 Å) and shift slightly outward displacement to accommodate Au–S bond formation. From the cluster surface to accommodate the directional geometry of the Au–S bond. This local distortion is consistent with the well-established chemisorption behaviour of thiol and thioether groups on gold surfaces, wherein which the strong Au–S interaction drives induce a local reconstruction of the Au surface coordination. It is also important to note that critically, the extent of Au cluster relaxation is not uniform across the five junctions. It is more pronounced in systems where the molecular HOMO energy lies closer to the Au Fermi level, as in $[DTBDT\text{-}DPP]_3$. This variation is physically relevant because the Au–S geometry directly modulates the electronic coupling Γ between the gold electrode states and the molecular frontier orbitals. Which, in turn, depends on the spatial overlap integral between the metal surface states and the frontier orbital density at the binding sulphur atom. A better-aligned and more distorted Au–S geometry increases this overlap, thereby lowering the effective charge-injection barrier. This is consistent with the smallest hole injection barrier observed for $[DTBDT\text{-}DPP]_3$ (Φ_h = 0.01–0.21 eV), where the HOMO at −5.31 eV aligns most closely with the Au Fermi level and the HOMO density is well delocalized toward the contact sulphur atoms, as confirmed by the isosurface plots in Fig. S1. In contrast, junctions such as $[DTBDT\text{-}BT]_3$, where the frontier orbital energies lie further from the Fermi level and the Au cluster geometry shows comparatively less distortion, exhibit higher injection barriers (Φ_h = 0.32–0.52 eV), consistent with weaker metal-molecule electronic coupling at those interfaces. In the $[PT]_{10}$ junction, the HOMO lies at −5.62 eV and the LUMO at −3.63 eV (Table 3). Against the Au Fermi level (E_F = −5.1 to −5.30 eV), these values give a hole injection barrier of Φ_h = 0.32–0.52 eV and an electron injection barrier of Φ_e = 1.47–1.67 eV. These are the largest injection barriers in the series, making $[PT]_{10}$ the poorest junction for charge injection. The macrocyclic molecules with DPP linkers exhibit a strong donor–acceptor phenomenon. $[DTBDT\text{-}DPP]_3$

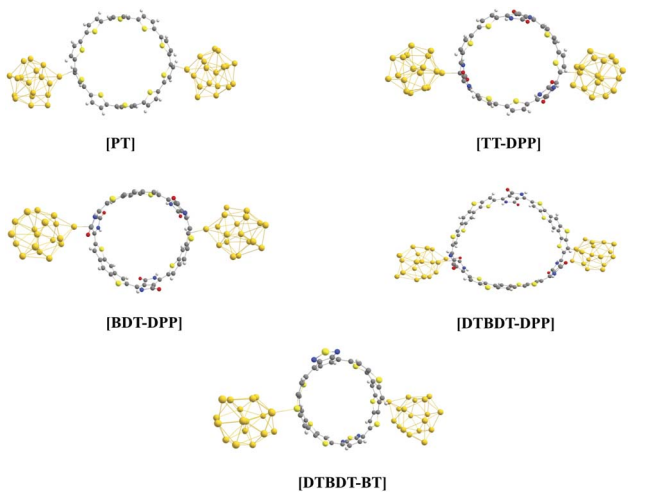

Fig. 4 Geometry-optimized molecular junctions of $[PT]_{10}$, $[TT\text{-}DPP]_3$, $[BDT\text{-}DPP]_3$, $[DTBDT\text{-}DPP]_3$, and $[DTBDT\text{-}BT]_3$ anchored to Au18 electrode clusters *via* Au–S bonds, calculated at the PBE0/GENECP level of theory.

Table 3 Representation of HOMO, LUMO, and energy bandgap of molecular junction of the molecules $[PT]_{10}$, $[TT\text{-}DPP]_3$, $[BDT\text{-}DPP]_3$, $[DTBDT\text{-}DPP]_3$, and $[DTBDT\text{-}BT]_3$

Compound	HOMO (eV)	LUMO (eV)	Energy (eV)
$[PT]_{10}$	−5.62	−3.63	1.98
$[TT\text{-}DPP]_3$	−5.56	−3.86	1.70
$[BDT\text{-}DPP]_3$	−5.56	−4.05	1.51
$[DTBDT\text{-}DPP]_3$	−5.31	−3.87	1.43
$[DTBDT\text{-}BT]_3$	−5.61	−3.67	1.93

has a HOMO at −5.31 eV, positioned within 0.01–0.21 eV of the Au Fermi level ($E_F = -5.1$ to −5.3 eV), giving the smallest hole injection barrier in the series ($\Phi_h = 0.01$–0.21 eV). The LUMO at −3.87 eV gives an electron injection barrier of $\Phi_e = 1.23$–1.43 eV. The small Φ_h identifies $[DTBDT\text{-}DPP]_3$ as the most efficient junction for hole injection, while the large Φ_e indicates that electron injection remains unfavourable across all five junctions studied. On the other hand, $[BDT\text{-}DPP]_3$ has a LUMO energy level of −4.05 eV. Although this lies closer to the Au Fermi level than any other molecule in the series, it remains above the E_F, giving an electron injection barrier of $\Phi_e = 1.05$–1.25 eV, the smallest Φ_e among the five junctions. The HOMO at −5.57 eV gives the hole injection barrier $\Phi_h = 0.25$–0.47 eV. Among the five molecules, $[BDT\text{-}DPP]_3$ offers the most favourable conditions for electron injection, though the barrier remains substantial. $[DTBDT\text{-}BT]_3$ has a HOMO at −5.646 eV, giving a hole injection barrier $\Phi_h = 0.32$–0.52 eV comparable to $[PT]_{10}$ and the largest among the d–a junctions. The LUMO at −3.678 eV gives an electron injection barrier $\Phi_e = 1.42$–1.62 eV, with both barriers among the highest in the series, $[DTBDT\text{-}BT]_3$ is the least efficient D–A junction for the charge injection. Thus, the incorporation of D–A moieties modulates the frontier orbital energies. From the Table 3, the HOMO and LUMO energies for all five junctions, from which the hole and electron injection barriers are calculated as $\Phi_h = |E_{HOMO} - E_F|$ and $\Phi_e = |E_{LUMO} - E_F|$, respectively. For hole injection, $[DTBDT\text{-}DPP]_3$ gives the small barrier ($\Phi_h = 0.01$–0.21 eV), followed by $[TT\text{-}DPP]_3$ ($\Phi_h = 0.26$–0.46 eV) and $[BDT\text{-}DPP]_3$ ($\Phi_h \approx 0.27$–0.47 eV). For electron injection, $[BDT\text{-}DPP]_3$ gives the smallest barrier ($\Phi_e = 1.05$–1.25 eV) owing to LUMO at −4.052 eV, though this barrier remains substantial across all five junctions. These injection barrier values are physically meaningful quantities that govern charge injection efficiency at the metal-molecule interface and provide a quantitative basis for evaluating it across the five metal-molecule junctions. Hole and electron injection barriers are calculated as $\Phi_h = |E_{HOMO} - E_F|$ and $\Phi_e = |E_{LUMO} - E_F|$, respectively, using the Au work function $E_F = -5.1$ to −5.3 eV. A smaller Φ value indicates a lower barrier and more efficient injection. $[DTBDT\text{-}DPP]_3$ gives the smallest hole injection barrier in the series at $\Phi_h = 0.1$–0.21 eV, indicating that the energetic barrier to hole injection from the Au electrode into $[DTBDT\text{-}DPP]_3$ is negligible at this level of theory. In contrast, $[DTBDT\text{-}BT]_3$ exhibits a higher injection barrier of 0.3–0.5 eV due to its largest HOMO value of −5.61 eV, thereby impeding hole transport efficiency. Similarly, the LUMO alignment is crucial for electron injection and n-type charge transport. In our study, $[BDT\text{-}DPP]_3$ enables efficient electron injection from the Fermi level, owing to its deepest LUMO at −4.05 eV. Although the LUMO of $[BDT\text{-}DPP]_3$ at −4.052 eV remains above E_F, the electron injection barrier of $\Phi_e = 1.05$–1.25 eV is the smallest in the series, making $[BDT\text{-}DPP]_3$ the most favourable junction for electron injection among the five systems studied. The moderate LUMO levels of the remaining molecules (−3.63 to −3.87 eV) lead to higher electron injection barriers, thereby reducingelectron transport.

The Au cluster geometric relaxation at the binding site, which has been discussed above, further reinforces this coupling by optimizing the Au–S bond geometry and increasing the metal-molecule orbital overlap at the contact. The spatial distribution of frontier orbitals affects the molecular overlap with electrode states. It determines the coupling strength; frontier orbitals that extend toward the Au–S contact site provide stronger electronic coupling and more efficient charge injection compared to localized orbitals. The frontier orbital density concentrated at the Au–S binding governs the electronic coupling (Γ) and, consequently, the charge injection efficiency across the metal-molecule interface. The HOMO and LUMO isosurface plots for the isolated macrocycles (SI, Fig. S1) confirm that meaningful frontier orbital density is present at the terminal sulphur atoms in all five systems, establishing that the illustrated Au–S contact geometry does not suffer from the vanishing orbital density at the binding site. Among the five, $[DTBDT\text{-}DPP]_3$ shows the most spatially extended HOMO delocalization across the donor units toward the anchor sulphur atoms, consistent with the stronger electronic coupling at the Au–S interface. The favourable HOMO alignment of $[DTBDT\text{-}DPP]_3$ with the Au Fermi level, combined with its narrow HOMO–LUMO gap and extended orbital density at the contact site, identifies it as the strongest candidate in the series for p-type hole injection. We also note that the macrocycles with multiple thiophene sulphur atoms along the ring could, in principle, form Au–S contacts at positions other than those shown in the idealized junction geometry of Fig. 6, potentially creating shorter through-bond transport pathways. Exploring these alternative binding geometries systematically represents a valuable direction for future work.

Fig. 5 shows the frontier molecular orbitals (HOMO and LUMO) of the macrocyclic molecules, which are sandwiched between gold nanoclusters (Fig. 6). In quantum mechanics, the charge density is proportional to $|\psi|^2$, which means both red (+) and blue (−) regions have equal probability of containing electron density. The red and blue lobes represent the wavefunction. From Fig. 5, the molecule $C[PT]_{10}$ shows a higher HOMO–LUMO band gap (1.98 eV), with orbital density mainly distributed on the macrocyclic molecule rather than on the gold cluster. The orbital distribution exhibits less delocalization. The HOMO is strongly localized in the macrocyclic structure (−5.62

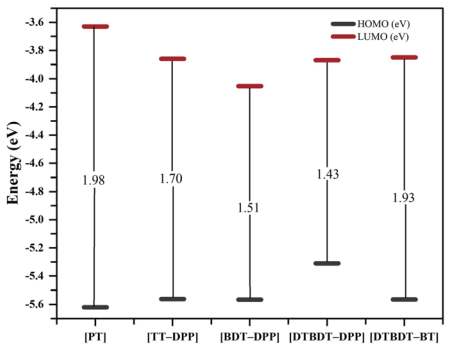

Fig. 5 HOMO and LUMO energy levels of the five macrocyclic molecular junctions, derived from PBE0/GENECP geometry optimized structures of $[PT]_{10}$, $[TT\text{-}DPP]_3$, $[BDT\text{-}DPP]_3$, $[DTBDT\text{-}DPP]_3$, and $[DTBDT\text{-}BT]_3$ anchored to Au18 marks decahedron electrode clusters.

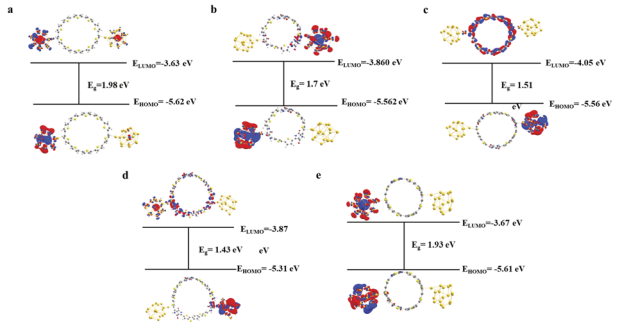

Fig. 6 Iso surface value of molecular junction (a) C[PT]$_{10}$ (b) C[TT-DPP]$_3$ (c) C[BDT-DPP]$_3$ (d) C[DTBDT-DPP]$_3$ (e) C[DTBDT-BT]$_3$ (iso surface value: 0.025).

eV) while the LUMO (−3.63 eV) shows the minimal hybridization with the gold cluster. On the other hand, the C[TT-DPP]$_3$ exhibits a reduced bandgap of 1.70 eV, indicating improved π-electron delocalization. The [TT-DPP]$_3$ D–A architecture reduces the HOMO–LUMO gap to 1.70 eV, compared with [PT]$_{10}$ (1.98 eV), consistent with stronger D–A coupling. The HOMO at −5.562 eV sits within 0.26–0.46 eV of the Au Fermi level, giving a hole injection barrier of Φ_h = 0.26–0.46 eV smaller than that of [PT]$_{10}$. The C[BDT-DPP]$_3$ structure exhibits the orbital delocalization with the narrower energy bandgap (1.51 eV). The benzodithiophene (BDT) units with DPP acceptors generate the extended π-conjugation. The LUMO (−4.052 eV) is significantly lowered, making it an excellent electron acceptor.

The HOMO (−5.566 eV) remains the same as in the DPP system, with better spatial distribution. Meanwhile, C[DTBDT-DPP]$_3$ shows a lower energy bandgap of 1.43 eV and the most effective intramolecular charge transfer. The DTBDT donor, in linkage with DPP acceptor units, created a strong D–A unit. The HOMO at −5.31 eV gives the smallest hole injection barrier in the series (Φ_h = 0.01–0.21 eV), while the LUMO at −3.87 eV gives an electron injection barrier of Φ_e = 1.23–1.43 eV, indicating that hole injection is energetically favoured over the electron injection in this junction. On the other hand, the molecule DTBDT, incorporating benzothiazole (BT) as the acceptor unit, shows a moderate bandgap of 1.702 eV. The orbital distribution shows significant asymmetry between HOMO and LUMO, with the LUMO showing better delocalization. The frontier orbital levels of [DTBDT-BT]$_3$ (HOMO −5.616 eV, LUMO −3.678 eV) give hole and electron injection barriers of Φ_h = 0.32–0.52 eV and Φ_e = 1.42–1.62 eV, respectively, among the highest in the series. Among the DPP-based macrocycles, [DTBDT-DPP]$_3$ shows the most favourable metal-molecule energy level alignment, with the smallest hole injection barrier and the narrowest HOMO–LUMO gap. These molecular-level electronic structure properties establish [DTBDT-DPP]$_3$ as the strongest candidate in this series for further experimental investigation.[9]

Conclusions

This study presents a systematic DFT analysis of the electronic structure and metal-molecule energy-level alignment in five radially conjugated macrocyclic systems and their linear counterparts, incorporating thiophene-based donor units and DPP or BT acceptor units. Macrocyclization produces a system-specific change in the HOMO–LUMO gap: ring closure narrows the gap in [BDT-DPP]$_3$, [DTBDT-DPP]$_3$, and [DTBDT-BT]$_3$ relative to their linear counterparts, whereas it widens the gap in [PT]$_{10}$ and [TT-DPP]$_3$. This divergence reflects the competing effects of ring strain, which disrupts π-orbital overlap and D–A coupling, thereby stabilizing the LUMO and destabilizing the HOMO. Among the five systems, [DTBDT-DPP]$_3$ exhibits the smallest HOMO–LUMO gap (1.44 eV in the junction model) and the most favourable alignment with the Au Fermi level, with a hole injection barrier of Φ_h = 0.01–0.21 eV. Modelling the macrocycle between Au18 electrode clusters establishes a well-defined framework for evaluating frontier orbital alignment and charge injection barriers (Φ_h, Φ_e) at the metal-molecule interface, both molecular-level quantities relevant to organic semiconductor device physics. The structure–property relationships established here provide a computational basis for identifying D–A macrocyclic candidates that warrant further experimental synthesis and characterization, and the junction geometries established in this work provide a starting point for future Landauer conductance calculations using NEGF-DFT methods.

Author contributions

M. K. R. and S. M. conceptualized the project, S. G. and K. R. performed the computational work and analysis. All authors contributed to the article's writing.

Conflicts of interest

There are no conflicts to declare.

Data availability

The data supporting this article have been included as part of the supplementary information (SI). The SI includes the computational procedure protocol, basis set comparisons, HOMO/LUMO isosurface plots, gold nanocluster analysis, optimized molecular junction geometries with Au–S bond distances, and full Cartesian coordinates for all linear and macrocyclic molecules, molecular junctions, and gold clusters. All DFT calculations were performed using the Gaussian software package, which is available commercially at https://gaussian.com. Supplementary information: (1) a detailed computational procedure protocol describing the DFT methodology, basis sets, and software used; (2) a comparison of SZP and DZP basis sets for modelling metal–molecule contacts; (3) HOMO and LUMO isosurface representations of all five macrocyclic molecules ([PT]$_{10}$, [TT-DPP]$_3$, [BDT-DPP]$_3$, [DTBDT-DPP]$_3$, and [DTBDT-BT]$_3$) calculated at the PBE0/6-31G** level; (4) a comparative analysis of gold nanocluster models and the selection of the Au$_{18}$ Marks decahedron cluster as the electrode model, including a table of HOMO, LUMO, and band gap values for eight candidate gold clusters;

(5) optimized geometries of the five molecular junctions with Au–S bond distances; and (6) full Cartesian coordinates of the linear and macrocyclic molecules, the Au_{18}-anchored molecular junctions, and the gold clusters. See DOI: https://doi.org/10.1039/d6ra01456a.

Acknowledgements

MKR and SM acknowledge SERB (DST, GoI) for ECR/2017/001937, & ANRF (DST, GoI) for CRG/2023/000978 and SRM University AP for Seed research grant SRMAP/URG/E&PP/2023-24/004. MKR and SM acknowledge the High-Performance Computing (HPC) facility at SRM University AP. KR and SG acknowledge the doctoral fellowship support from SRM University AP.

References

1 D. An, R. Zhang, J. Zhu, T. Wang, Y. Zhao, X. Lu and Y. Liu, *Chem. Sci.*, 2024, **15**, 4590–4601.
2 X. Zhang, Y. Xu and P. Du, *Acc. Mater. Res.*, 2025, **6**, 399–410.
3 E. R. Darzi and R. Jasti, *Chem. Soc. Rev.*, 2015, **44**, 6401–6410.
4 C. Zhong, Y. Yan, Q. Peng, Z. Zhang, T. Wang, X. Chen, J. Wang, Y. Wei, T. Yang and L. Xie, *Nanomaterials*, 2023, **13**, 1750.
5 J. M. Dos Santos, L. K. Jagadamma, J. Cameron, A. A. Wiles, C. Wilson, P. J. Skabara, I. D. W. Samuel and G. Cooke, *J. Mater. Chem. C*, 2021, **9**, 16257–16271.
6 A. L. Kanibolotsky, N. J. Findlay and P. J. Skabara, *Beilstein J. Org. Chem.*, 2015, **11**, 1749–1766.
7 F. Dikcal, T. Ozturk and M. E. Cinar, *Org. Commun.*, 2017, **10**, 56–71.
8 L. Vallan, E. Istif, I. J. Gómez, N. Alegret and D. Mantione, *Polymers*, 2021, **13**, 1–49.
9 S. Haseena and M. K. Ravva, *Sci. Rep.*, 2022, **12**, 1–19.
10 C. Li, C. Wang, Y. Guo, Y. Jin, N. Yao, Y. Wu, F. Zhang and W. Li, *J. Mater. Chem. C*, 2019, **7**, 3802–3810.
11 M. Adnan, M. Kashif, Z. Irshad, R. Hussain, H. W. Darwish and J. Lim, *Spectrochim. Acta, Part A*, 2024, **320**, 12461.
12 L. Ma, Z. Li, B. Chen, X. Zheng, H. Xie, C. Ji, X. Zhan, Y. Liu and X. Chen, *Org. Electron.*, 2023, **122**, 106909.
13 C. Liu, L. Yin, Y. Guo, B. Xie, X. Wang and Y. Li, *Mater. Adv.*, 2023, **5**, 762–776.
14 A. Carella, A., M. Landi, F. Bonomo, R. Chiarella, A. Centore, S. Peluso, M. Nejrotti and M. Barra, *Molecules*, 2024, **29**, 2805.
15 M. Makala, M. Barłóg, D. Dremann, S. Attar, E. G. Fernández, M. Al-Hashimi and O. D. Jurchescu, *J. Mater. Chem. C*, 2024, **12**, 17089–17098.
16 A. Ghobadi, C. J. Mathai, J. Cook, G. Bian, S. Attar, M. Al-Hashimi, S. Gangopadhyay and S. Guha, *Adv. Electron. Mater.*, 2025, **11**, 1–9.
17 A. Tang, C. Zhan, J. Yao and E. Zhou, *Adv. Mater.*, 2017, 1600013.
18 S. Alam and J. Lee, *Molecules*, 2023, **28**(7), 3171.
19 J. Zhu, M. Du, A. Tang, Y. Meng, C. Li, Q. Guo and E. Zhou, *J. Mater. Chem. C*, 2024, **12**, 12971–12979.
20 M. Wei and D. F. Perepichka, *J. Mater. Chem. A*, 2025, **13**, 12785–12807.
21 K. Kranthiraja, W. He, H. W. Yu, Z. Feng, N. Nozaki, H. Matsumoto, M. H. Yu, Y. Li, S. Manzhos, M. R. Andersson, C. C. Chueh, T. Michinobu and P. Sonar, *Sol. RRL*, 2024, **8**, 1–11.
22 F. A. Aloufi, R. F. Halawani, B. Jamoussi, A. K. Hajri and N. Zahi, *ACS Omega*, 2023, **8**, 21425–21437.
23 A. Abdelkhalk, C. Mustafa, E. A. Siham, E. B. Morad, E. Benachir, E. Idrissi Mohammed and L. Said, *Mater. Sci. Energy Technol.*, 2023, **6**, 137–144.
24 M. Lim, X. Ma, Y. Kang, M. H. Jee, S. Lee, S. Y. Jeong, T. H. Kim, J. W. Shim, F. Zhang and H. Y. Woo, *Chem. Eng. J.*, 2025, **504**, 158769.
25 C. B. Nielsen, S. Holliday, H. Y. Chen, S. J. Cryer and I. McCulloch, *Acc. Chem. Res.*, 2015, **48**, 2803–2812.
26 A. Khalid, R. A. Khera, A. Saeed, M. Khalid, S. Iqbal and J. Iqbal, *Optik*, 2021, **228**, 1–11.
27 R. Bhattacharjee, J. D. Tovar and M. Kertesz, *Chem. Sci.*, 2025, **16**, 14595–14604.
28 P. Seitz, M. Bhosale, L. Rzesny, A. Uhlmann, J. S. Wössner, R. Wessling and U. B. Esser, *Angew. Chem., Int. Ed.*, 2023, **135**(43), e202306184.
29 N. S. Shaikh, V. C. Lokhande, P. Pansa-Ngat, S. Ubale, J. S. Shaikh, S. Praserthdam, S. R. Sabale, C. D. Lokhande, T. Ji and P. Kanjanaboos, *Energy Fuels*, 2022, **36**, 2799–2810.
30 M. J. Frisch, G. W. Trucks, H. B. Schlegel, G. E. Scuseria, M. A. Robb and J. R. Cheeseman *et al.*, *Gaussian 16, Revision C.01*, Gaussian, Inc., Wallingford, CT, 2019.
31 H. Yi, X. Qin, L. Zhai, H. Duan, H. Chen, Y. Zuo, X. Lian, K. Tian, J. Zhang, Z. Liu and P. Xu, *Precis. Chem.*, 2023, **1**, 548–554.
32 M. K. Charyton, T. Reiker, K. Kotwica, M. Góra, H. Zacharias and N. D. Boscher, *Mater. Adv.*, 2023, **4**, 2625–2635.
33 S. Góger, L. M. Sandonas, C. Müller and A. Tkatchenko, *Phys. Chem. Chem. Phys.*, 2023, **25**, 22211–22222.
34 M. Khalid, S. Naz, K. Mahmood, S. Hussain, A. A. Carmo Braga, R. Hussain, A. H. Ragab and S. R. Al-Mhyawi, *RSC Adv.*, 2022, **12**, 31192–31204.
35 O. T. Hofmann, E. Zojer, L. Hörmann, A. Jeindl and R. J. Maurer, *Phys. Chem. Chem. Phys.*, 2021, **23**, 8132–8180.
36 S. Shi, M. Wan, Z. Fan, K. Diao and D. Chen, *Comput. Theor. Chem.*, 2024, **1238**, 1–10.
37 T. Mori and T. Hegmann, *J. Nanopart. Res.*, 2016, **18**, 1–36.
38 S. Y. Quek, M. M. Biener, J. Biener, J. Bhattacharjee, C. M. Friend, U. V Waghmare and E. Kaxiras, *J. Chem. Phys.*, 2007, **127**, 104704.
39 Y. Meir and N. S. Wingreen, *Phys. Rev. Lett.*, 1992, **68**, 2512–2515.
40 X. Yuan, J. Li, W. Deng, X. Zhou and C. Duan, *Chem. Sci.*, 2025, **16**, 14424–14447.
41 T. P. Kaloni, P. K. Giesbrecht, G. Schreckenbach and M. S. Freund, *Chem. Mater.*, 2017, **29**, 10248–10283.
42 P. Meti, H. H. Park and Y. D. Gong, *J. Mater. Chem. C*, 2020, **8**, 352–379.

43 W. Zhuang, S. Wang, Q. Tao, W. Ma, M. Berggren, S. Fabiano, W. Zhu and E. Wang, *Macromolecules*, 2021, **54**, 970–980.
44 Z. Jiang and Y. Kuninobu, *Chem. Commun.*, 2024, **60**, 7642–7645.
45 O. El Bakouri, D. W. Szczepanik, K. Jorner, R. Ayub, P. Bultinck, M. Solà and H. Ottosson, *J. Am. Chem. Soc.*, 2022, **144**, 8560–8575.
46 W. Shi, M. Wang, L. Venkataraman and J. D. Tovar, *Nano Lett.*, 2025, **25**(31), 12101–12106.